

Emergent interaction-induced topology in Bose-Hubbard ladders

David Wellnitz,^{1,2} Gustavo A. Domínguez-Castro,³ Thomas Bilitewski,⁴
Monika Aidelsburger,^{5,6,7} Ana Maria Rey,^{1,2} and Luis Santos³

¹*JILA, National Institute of Standards and Technology and Department of Physics,
University of Colorado, Boulder, CO, 80309, USA*

²*Center for Theory of Quantum Matter, University of Colorado, Boulder, CO, 80309, USA*

³*Institut für Theoretische Physik, Leibniz Universität Hannover, Appelstrasse 2, D-30167 Hannover, Germany*

⁴*Department of Physics, Oklahoma State University, Stillwater, Oklahoma 74078, USA*

⁵*Max-Planck-Institut für Quantenoptik, Hans-Kopfermann-Strasse 1, 85748 Garching, Germany*

⁶*Fakultät für Physik, Ludwig-Maximilians-Universität, Schellingstrasse 4, 80799 München, Germany*

⁷*Munich Center for Quantum Science and Technology (MCQST), Schellingstraße 4, 80799 München, Germany*
(Dated: September 10, 2024)

We investigate the quantum many-body dynamics of bosonic atoms hopping in a two-leg ladder with strong on-site contact interactions. We observe that when the atoms are prepared in a staggered pattern with pairs of atoms on every other rung, singlon defects, i.e. rungs with only one atom, can localize due to an emergent topological model, even though the underlying model in the absence of interactions admits only topologically trivial states. This emergent topological localization results from the formation of a zero-energy edge mode in an effective lattice formed by two adjacent chains with alternating strong and weak hopping links (Su-Schrieffer-Heeger chains) and opposite staggering which interface at the defect position. Our findings open the opportunity to dynamically generate non-trivial topological behaviors without the need for complex Hamiltonian engineering.

Topological phases of matter [1, 2], including the quantum Hall effect [3–5] and topological insulators [6, 7] have attracted significant attention for quantum science and technologies [8–11] given their robustness against disorder and defects. While non-interacting topological phases have been realized in a broad range of settings, both classical [12–15] and quantum [16–25], and are to a great extent well understood [26, 27], interaction-enabled topological states remain largely unexplored. Understanding how topological phases may arise in interacting systems is hence an exciting, but challenging problem.

Ultra-cold gases [28–31] with tunable interactions in optical lattices and tweezer arrays [32] are emerging as an excellent platform to shed light on this direction [25, 33, 34], in particular with their capability to observe many-body states with single-site and spin resolution [35–42]. These have allowed the realization of non-interacting topological phases and observation of key underlying features [17–23], such as edge states and currents [17–19, 43], Chern numbers [21], and topological pumping [22, 23]. Progress towards the implementation of interacting systems such as many-body symmetry protected topological phases [2] include bosonic Su-Schrieffer-Heeger (SSH) models [44] in interacting Rydberg atoms [45], a fractional quantum Hall state with few atoms [46, 47], and the Haldane phase in Fermi-Hubbard ladders [48, 49]. However, especially for mobile particles, reaching the ultracold temperature necessary to observe interacting topological ground states remains a significant obstacle. While internal degrees of freedom can be pumped into a single state with essentially zero entropy, similar techniques do not exist for motion in lattices. It would be hence highly appealing to find settings where

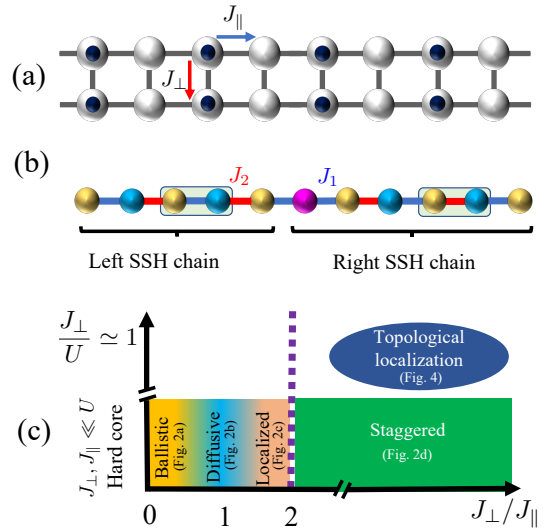


FIG. 1. (a) Bose-Hubbard ladder with rung (leg) hopping J_{\perp} (J_{\parallel}). Initially there is one (no) particle per site in even (odd) rungs. (b) Emergent SSH chains of opposite staggering interface at a central site (purple), and emergent model in the dynamics of singlon defects. (c) Overview of the regimes. In the hard-core regime, $J_{\perp}, J_{\parallel} \ll U$, rung density-density (RDD) correlations are negative, and their expansion within relevant time scales transitions from ballistic to diffusive to localized when $\eta \equiv J_{\perp}/J_{\parallel}$ grows from 0 to 2. For $\eta > 2$, staggered RDD correlations expand ballistically. For $J_{\parallel} \ll J_{\perp} \lesssim U$, singlon defects experience topological or non-topological localization. We indicate which figures illustrate the regimes.

topology emerges naturally in the dynamics of a strongly interacting system [28–31, 50, 51] from an easy to prepare initial state.

In this Letter, we report on emerging interaction-induced topological localization in an experimentally accessible system of strongly interacting bosons in two-leg ladders. Two-leg ladders have played a major role as model systems for quantum magnetism [52, 53], in non-equilibrium many-body dynamics, hydrodynamics and transport [54–58], and in realizations of synthetic magnetism [17]. More recently, bosons in optical ladders have been used to study non-equilibrium dynamics in the hard-core limit where strong interactions prevent more than one atom per site (a model equivalent to an XX spin ladder [54]). By initially preparing a density wave (DW) along the legs with filled (empty) sites in even (odd) rungs (Fig. 1 (a)), experiments have observed within their accessible time scales a crossover from ballistic to diffusive correlation dynamics when the rung hopping (J_{\perp}) increases from zero to equal to the leg hopping (J_{\parallel}) [59].

Here we analyze the opposite regime when $\eta \equiv J_{\perp}/J_{\parallel} \gg 1$, focusing on experimentally accessible time scales. Besides radically different correlations in the hard-core limit, we find that, surprisingly, when the on-site interactions are large but finite, an initial isolated singlon defect in the DW pattern, i.e. a singly-occupied rung, experiences an emergent effective lattice composed of two SSH chains of opposite staggering, and hence different topology, that meet at the initial defect position (Fig. 1 (b)). These interfaces can feature two distinct types of localized states resulting in the localization of defects: (i) zero energy edge modes related to the SSH topology, and (ii) energetically bound states at the ends of the energy spectrum. Our analysis hence unveils a surprising link between topology and many-body dynamics in strongly interacting ladders. Contrary to other realizations of topological models in optical lattices [45, 49, 60], or topological interfaces of SSH chains in other systems [61–64], the SSH chain and the topological interface are not externally implemented, but emerge naturally from the interplay of interactions, motion and the original DW pattern. This intriguing physics (Fig. 1 (c)) can be probed in on-going experiments.

Model.— We consider bosons in a square ladder, see Fig. 1 (a), with legs 1 and 2, described in the tight-binding regime by the Bose-Hubbard (BH) Hamiltonian $\hat{H} = \hat{H}_0 + \frac{U}{2} \sum_{i,\alpha} \hat{n}_{i,\alpha} (\hat{n}_{i,\alpha} - 1)$, with

$$\hat{H}_0 = - \sum_i \left(\frac{J_{\parallel}}{2} \sum_{\alpha=1,2} \hat{b}_{i+1,\alpha}^{\dagger} \hat{b}_{i,\alpha} + \frac{J_{\perp}}{2} \hat{b}_{i,1}^{\dagger} \hat{b}_{i,2} + \text{H.c.} \right), \quad (1)$$

where $\hat{b}_{i,\alpha}$ is the bosonic operator at site i of leg α , $\hat{n}_{i,\alpha} = \hat{b}_{i,\alpha}^{\dagger} \hat{b}_{i,\alpha}$, and U characterizes the on-site interactions. Motivated by recent experiments [59] we assume large U , and consider an initial DW, in which sites at even (odd) rungs are occupied by one (no) atom.

Hard-core regime.— To develop an intuition of the dynamical regimes, we first consider an idealized scenario without initial defects in the DW. Furthermore,

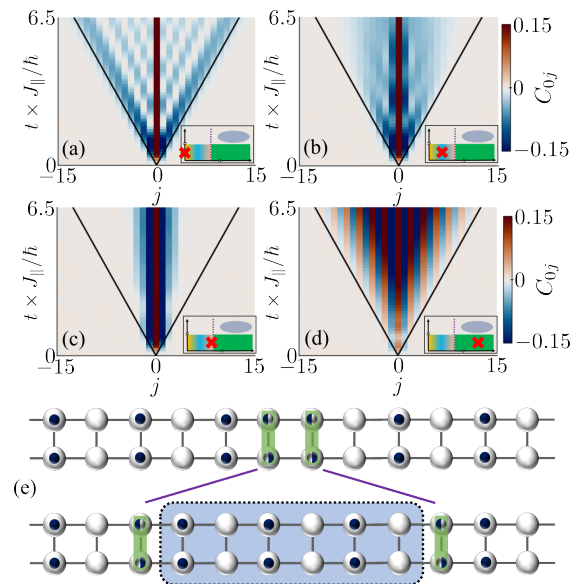


FIG. 2. Time evolution of the RDD correlation C_{0j} with $\eta = 0$ (a), $\eta = 1$ (b), $\eta = 2$ (c) and $\eta = 8$ (d). Simulations of the hard-core Hamiltonian \hat{H}_0 on 31 sites, using MPS with bond dimensions $\chi = 1536$ (a/b), 1024 (c), 512 (d). The black lines correspond to the ballistic propagation when $\eta = 0$. The red “x” in the insets locates the plots in Fig. 1(c). (e) Mechanism leading to the staggered correlations in (d). Quantum fluctuations result in pairs of singlon defects (green), which when moving apart form a string of rungs (blue shaded area) with an inverted DW compared to the initial one.

we restrict the dynamics to the hard-core manifold described solely by \hat{H}_0 for very large $U \gg J_{\perp}, J_{\parallel}$. A Bogoliubov stability analysis shows that the DW is stable against the exponential proliferation of singlon defects if $\eta > 2$ (see [65]). Indeed, $\eta \simeq 2$ marks the onset of clearly different dynamics. As in recent experiments [59], we consider rung density-density (RDD) correlations $C_{ij} = \langle \hat{n}_i \hat{n}_j \rangle - \langle \hat{n}_i \rangle \langle \hat{n}_j \rangle$, with $\hat{n}_i = \hat{n}_{i,1} + \hat{n}_{i,2}$ the particle number operator of rung i . Our results of $C_{0j}(t)$, obtained using Matrix Product State (MPS) calculations, show a markedly different behavior for $\eta < 2$ than for $\eta > 2$. For $\eta = 0$ (Fig. 2 (a)), the system is integrable, and the correlations expand ballistically as $C_{0j}(t) = -\frac{1}{4} \mathcal{J}_j^2(2J_{\parallel}t/h)$, with \mathcal{J}_j the Bessel function of first kind. As discussed in Ref. [59], when η increases from 0 to 1 the expansion changes from ballistic to diffusive within the time scale of the experiments (Fig. 2 (b)). A further increase of η results in a strong slowdown of the evolution of the correlations, which within experimentally accessible time scales becomes clearly subdiffusive, and eventually approximately localized at $\eta = 2$ (Fig. 2 (c)). One would naively expect that the larger η the more localized C_{0j} would be. Interestingly, the nature of the correlations changes remarkably at $\eta \simeq 2$. Whereas $C_{0j} < 0$ for $\eta < 2$, for $\eta > 2$ RDD correlations are staggered, $(-1)^j C_{0j} > 0$,

and expand ballistically as for $\eta = 0$ (Fig. 2 (d)).

To understand these dynamics for $\eta \gg 1$, we introduce the hard-core rung states: $|2\rangle \equiv \begin{pmatrix} \bullet \\ \bullet \end{pmatrix}$, $|0\rangle \equiv \begin{pmatrix} \circ \\ \circ \end{pmatrix}$, and $|\pm\rangle \equiv \frac{1}{\sqrt{2}} \left[\begin{pmatrix} \bullet \\ \circ \end{pmatrix} \pm \begin{pmatrix} \circ \\ \bullet \end{pmatrix} \right]$, where \bullet (\circ) denotes an occupied (empty) site. Quantum fluctuations due to leg hopping create singlon-defect pairs (Fig. 2 (e)): $|2, 0\rangle \rightarrow |+, +\rangle - |-, -\rangle$, with a density $1/\eta^2$. These defects, initially at neighboring sites, drift apart with rate J_{\parallel} by position swaps between $|\pm\rangle$ and $|2\rangle$ or $|0\rangle$ induced by the leg hopping (Fig. 2 (e)). After a time t , the defects have a probability $\mathcal{J}_{r-1}^2(2J_{\parallel}t)$ to be at $r \geq 1$ sites apart [65]. The rungs in between the defects present an inverted DW pattern compared to the original one (Fig. 2 (e)), and the RDD correlations acquire the form [65]:

$$C_{0j}(t) \propto (-1)^j \left(\mathcal{J}_{j-1}^2(2J_{\parallel}t) + 4 \sum_{k>0} k \mathcal{J}_{k+j-1}^2(2J_{\parallel}t) \right), \quad (2)$$

which corresponds to the staggered correlations of Fig. 2 (d), which expand ballistically as for $\eta = 0$.

Effective SSH chain.— Up to this point we have considered the hard-core model (1). Large but finite U may however play an important and surprising role in the defect dynamics. Up to second order in $J_{\perp, \parallel}/U$, the (again hard-core) model becomes $\hat{H}_{\text{eff}} = \hat{H}_0 + \Delta\hat{H}$, where

$$\begin{aligned} \Delta\hat{H} = & -\frac{J_{\perp}^2}{U} \sum_j \hat{n}_{j,1} \hat{n}_{j,2} - \frac{J_{\parallel}^2}{U} \sum_{j,\alpha} \hat{n}_{j,\alpha} \hat{n}_{j+1,\alpha} \\ & - \frac{J_{\perp} J_{\parallel}}{2U} \sum_{j,\alpha,\beta \neq \alpha} \left[\hat{b}_{j+1,\beta}^{\dagger} (\hat{n}_{j+1,\alpha} + \hat{n}_{j,\beta}) \hat{b}_{j,\alpha} + \text{H.c.} \right] \\ & - \frac{J_{\parallel}^2}{2U} \sum_{j,\alpha} \left(\hat{b}_{j+2,\alpha}^{\dagger} \hat{n}_{j+1,\alpha} \hat{b}_{j,\alpha} + \text{H.c.} \right), \quad (3) \end{aligned}$$

with nearest-neighbor (NN) interactions along the legs and the rungs (first line), and collisionally-assisted hops along plaquette diagonals (second line), and between next-to-NN rungs (third line).

For $U = \infty$ leg-hopping induces the same swap rate for $|\pm\rangle$ with $|2\rangle$ or $|0\rangle$. For finite U , the interplay of leg hopping and collisionally-induced diagonal hopping causes $|\pm\rangle$ to swap with $|2\rangle$ at a rate $J_{\pm} = J_{\parallel} (1 \pm 2J_{\perp}/U)$, while $|\pm\rangle$ and $|0\rangle$ still swap at rate J_{\parallel} (Fig. 3 (a)). This is particularly relevant if, as typically in experiments, the initial DW presents isolated singlon defects. Consider a singlon defect at rung $j = 0$ in an otherwise perfect DW (Figs. 3 (b-c)). The defect experiences an effective staggered hopping described by the SSH Hamiltonian:

$$H_{\text{SSH}} = \frac{1}{2} \sum_j J_{j,j+1} (|\phi_j\rangle \langle \phi_{j+1}| + \text{H.c.}), \quad (4)$$

with $|\phi_j\rangle$ the state with the defect in rung j , and $J_{j,j+1} = J_1$ (J_2) for even (odd) j for $j \geq 0$, and the opposite

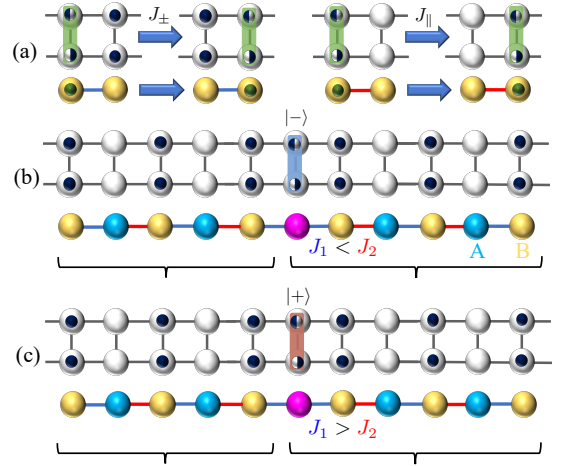


FIG. 3. (a) A singlon defect propagates by swapping its position with doubly-occupied and empty rungs. Due to finite U , these swaps result in two different hopping rates (blue and red lines). The defect propagates in an effective lattice in which the right and the left of the initial defect position present opposite SSH staggering, illustrated for the case of a defect in what should have been an empty rung. (b) For a $|-\rangle$ defect (blue), $J_1 < J_2$, and the defect experiences topological localization. (c) For a $|+\rangle$ (brown), $J_1 > J_2$, and the defect displays non-topological localization. In the effective chain, light blue (yellow) sites indicate the A (B) sublattice.

for $j < 0$. The defect moves in an effective lattice of two SSH chains with opposite staggering that meet at the initial defect position (Figs. 3 (b-c)). Since one SSH chain is topological and the other is not, an exponentially localized zero-energy mode appears at the interface [44, 61–64]. We call the sublattice of even rungs, where the defect is initially, A, and the sublattice of odd rungs B.

Topological and non-topological localization.— We consider first $J_1 < J_2$ (Fig. 3 (b)). This is the case in which a $|-\rangle$ ($|+\rangle$) defect occurs where $|0\rangle$ ($|2\rangle$) should have been, for which $J_1 = J_-$ (J_{\parallel}) and $J_2 = J_{\parallel}$ (J_+). At the interface between the SSH half-chains, the system presents a localized zero-energy edge mode [65], $|\psi\rangle = \sqrt{P_0} \sum_m e^{-|m|/2\xi} |\phi_{2m}\rangle$, with $\xi = \frac{1}{2\ln(J_2/J_1)}$, and $P_0 = |\langle \phi_0 | \psi \rangle|^2 = (J_2^2 - J_1^2)/(J_2^2 + J_1^2)$. The defect (initially in $|\phi_0\rangle$) remains hence localized with probability P_0 , and the localized population only occupies A rungs.

The situation changes radically if $J_1 > J_2$, which corresponds to a $|-\rangle$ ($|+\rangle$) defect where $|2\rangle$ ($|0\rangle$) should have been, for which $J_1 = J_{\parallel}$ (J_+) and $J_2 = J_-$ (J_{\parallel}). Topological localization is precluded because the zero-energy edge state has only support in the B sublattice [65]. However, localized states appear at the two ends of the spectrum [65], with opposite energies $\pm E$, with $E \simeq \frac{1}{2} \left[\sqrt{2}J_1 + \frac{J_2^2/4}{(\sqrt{2}-1)J_1} \right]$. The population of these localized states, results in partial localization of the defect, which oscillates with frequency $\Omega = E/\hbar$ between the A and B sublattices [65]. This may be intuitively un-

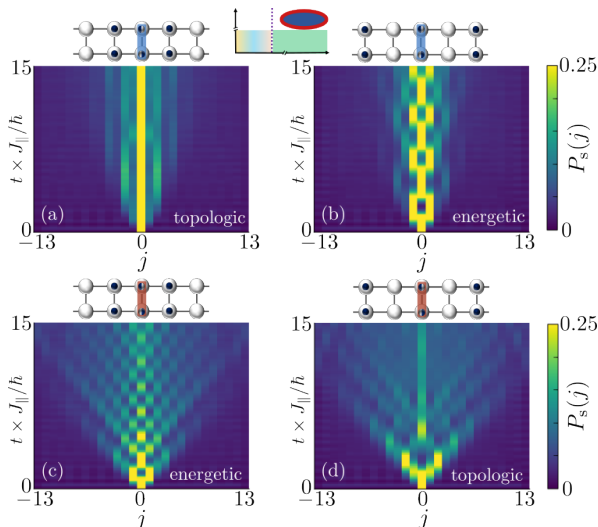


FIG. 4. Time evolution of the probability of finding the defect in rung j , $P_s(j)$. The color bar saturates above 0.25. The initial defect position and state is indicated on top of each panel, with a blue (brown) box indicating a $|-\rangle$ ($|+\rangle$) defect. The inset in the top locates this figure in Fig. 1(c). MPS simulations of the full Bose-Hubbard Hamiltonian \hat{H} with 27 sites, $\eta = 16$, $J_{\perp}/U = 1/2$, and bond dimension $\chi = 768$.

derstood from the case $J_2 \ll J_1$, for which the central A site and the symmetric superposition of the neighboring B sites form an isolated two-level system characterized by an oscillatory frequency $\Omega = \sqrt{2}J_1/2\hbar$.

Figure 4 shows the time evolution of the singlon defect probability $P_s(j)$ for $\eta = 16$ and $J_{\perp}/U = 0.5$ [66], for four different cases: topological localization in Figs. 4 (a) and (d), and non-topological localization in Figs. 4 (b) and (c). Note the strikingly distinct dynamics in both cases, with clear oscillations between sublattice A and B in the non-topological case. Although the localization mechanism and the defect dynamics differ in the two regimes, the localized fraction is in any case very significant as long as J_1 and J_2 are sufficiently different. Hence, irrespective of the defect created and where it is produced, if J_{\perp}/U is sufficiently large, we may expect strong localization of all singlon defects.

Other interaction-induced terms.— The emergent SSH chain experienced by the defects demands the stability of the DW for finite U and $J_{\parallel} \ll J_{\perp} < U$. Projecting H_{eff} on the manifold of states without singlon defects [67], we obtain an effective model for doubly-occupied rungs [65], $\hat{H}_D = \frac{3J_{\parallel}^2}{2U} \sum_j \left(\hat{d}_j^{\dagger} \hat{d}_{j+1} + \hat{d}_{j+1}^{\dagger} \hat{d}_j - \frac{10}{3} \hat{n}_{d,j} \hat{n}_{d,j+1} \right)$, with \hat{d}_j the (hard-core boson) annihilation operator of doubly-occupied rungs, and $\hat{n}_{d,j} = \hat{d}_j^{\dagger} \hat{d}_j$. The hopping terms in \hat{H}_D correspond to $|20\rangle \rightarrow |02\rangle$ swaps, which scramble the initial DW. Interestingly, the relatively strong NN interaction between doubly-occupied rungs makes the DW stable against those swaps [65]. Hence, quantum fluctuations of the DW order may lead for times $t > 2U/3J_{\parallel}^2$

to the blurring of the background, but they do not destroy the localization [65]. Furthermore, being hard-core bosons, singlon defects repel elastically [67]. NN interactions may lead to $|+, -\rangle \rightarrow |-, +\rangle$ swaps with a rate $J_{\parallel}^2/2U$, but these swaps are negligible for low defect densities [65]. Finally, collisionally-assisted next-to-NN hopping is only relevant due to hops $|\pm, 2, 0\rangle \rightarrow |0, 2, \pm\rangle$, which scramble the DW. These processes occur with a rate $-J_{\parallel}^2/2U$, being negligible for $t < 2U/J_{\parallel}^2$.

Experimental realization.— The emergent SSH chain experienced by each singlon defect is hence to a good approximation affected neither by the presence of neighboring defects, nor by quantum fluctuations of the DW or next-to-NN hops. Probing the regime $J_{\parallel} \ll J_{\perp} < U$ is readily accessible in on-going experiments [59]. Singlon-defect localization may be monitored in various ways. Current quantum gas microscopes [68] can deterministically create and measure $|+\rangle$ and $|-\rangle$ with single-rung resolution. The dynamics depicted in Fig. 4 can then be observed directly. Even without site-resolved state preparation, asymmetries in the defect creation between even and odd rungs can be used to access the localization dynamics. Under current experimental conditions [59] we expect that 80% of the created singlon defects are in even rungs, which should have been doubly occupied. One may hence monitor the imbalance $\mathcal{I} = 2\mathcal{N}_E - 1$, with \mathcal{N}_E the number of singly-occupied even rungs. For $U = \infty$, defects propagate ballistically and $\mathcal{I}(t) = \mathcal{I}(0)\mathcal{J}_0(2J_{\parallel}t/\hbar)$. In contrast, topological and non-topological localization should result in a markedly different $\mathcal{I}(t)$, since topologically localized defects do not oscillate between sublattices, and non-topological defects oscillate between them with a frequency Ω .

Conclusions.— Bose-Hubbard ladders initialized in a density wave provide an unexpected platform for the realization of an emergent interaction-enabled topological-non-topological interface of two SSH chains with opposite staggering, without the necessity of tailored external potentials. As a result, singlon defects experience two possible localization mechanisms, one topological and the other non-topological, characterized by strikingly distinct dynamics. This surprising link between topology and many-body quantum dynamics can be probed in ongoing experiments. In a broader context, our work illustrates how defect dynamics is determined by the background substrate they move through (here a density wave). This idea readily generalizes to different static backgrounds, e.g. a random background may result in localization without external disorder akin to disorder-free localization [69], and to dynamically coupled backgrounds, e.g. in bilayer settings defect motion reconfigures the initial state pattern and hence the effective tunnelling rates. Our results also open further intriguing perspectives for the realization of emergent topological behavior in other platforms, in particular in synthetic ladders created using internal states [18, 19, 70].

Acknowledgements We acknowledge careful reading of the manuscript by Joanna Lis and Raphael Kaubrueger. G.A.D.-C. and L.S. acknowledge the support of the Deutsche Forschungsgemeinschaft (DFG, German Research Foundation) – Project-ID 274200144 – SFB 1227 DQ-mat within the project A04, and under Germany’s Excellence Strategy – EXC-2123 Quantum-Frontiers – 390837967). A.M.R. and D.W. acknowledge funding from AFOSR MURI Grant FA9550-21-1-0069, ARO W911NF-24-1-0128, NSF JILA-PFC PHY-2317149, OMA-2016244, the U.S. Department of Energy, Office of Science, National Quantum Information Science Research Centers, Quantum Systems Accelerator and NIST. M.A. acknowledges funding from the Deutsche Forschungsgemeinschaft (DFG, German Research Foundation) via Research Unit FOR5522 under project number 499180199, via Research Unit FOR 2414 under project number 277974659 and under Germany’s Excellence Strategy – EXC-2111 – 390814868 and funding under the Horizon Europe programme HORIZON-CL4-2022-QUANTUM-02-SGA via the project 101113690 (PASQuanS2.1).

-
- [1] X.-G. Wen, Colloquium: Zoo of quantum-topological phases of matter, *Rev. Mod. Phys.* **89**, 041004 (2017).
- [2] T. Senthil, Symmetry-protected topological phases of quantum matter, *Annual Review of Condensed Matter Physics* **6**, 299 (2015).
- [3] R. E. Prange and S. M. Girvin, eds., *The Quantum Hall Effect* (Springer, New York, NY, 1990).
- [4] K. von Klitzing, T. Chakraborty, P. Kim, V. Madhavan, X. Dai, J. McIver, Y. Tokura, L. Savary, D. Smirnova, A. M. Rey, C. Felser, J. Gooth, and X. Qi, 40 years of the quantum hall effect, *Nature Reviews Physics* **2**, 397–401 (2020).
- [5] C.-Z. Chang, C.-X. Liu, and A. H. MacDonald, Colloquium: Quantum anomalous hall effect, *Rev. Mod. Phys.* **95**, 011002 (2023).
- [6] M. Z. Hasan and C. L. Kane, Colloquium: Topological insulators, *Rev. Mod. Phys.* **82**, 3045 (2010).
- [7] X.-L. Qi and S.-C. Zhang, Topological insulators and superconductors, *Rev. Mod. Phys.* **83**, 1057 (2011).
- [8] H. Luo, P. Yu, G. Li, and K. Yan, Topological quantum materials for energy conversion and storage, *Nature Reviews Physics* **4**, 611–624 (2022).
- [9] M. J. Gilbert, Topological electronics, *Communications Physics* **4**, 10.1038/s42005-021-00569-5 (2021).
- [10] O. Breunig and Y. Ando, Opportunities in topological insulator devices, *Nature Reviews Physics* **4**, 184–193 (2021).
- [11] C. Nayak, S. H. Simon, A. Stern, M. Freedman, and S. Das Sarma, Non-abelian anyons and topological quantum computation, *Rev. Mod. Phys.* **80**, 1083 (2008).
- [12] J. Ningyuan, C. Owens, A. Sommer, D. Schuster, and J. Simon, Time- and site-resolved dynamics in a topological circuit, *Phys. Rev. X* **5**, 021031 (2015).
- [13] M. Hafezi, S. Mittal, J. Fan, A. Migdall, and J. M. Taylor, Imaging topological edge states in silicon photonics, *Nature Photonics* **7**, 1001–1005 (2013).
- [14] P. St-Jean, V. Goblot, E. Galopin, A. Lemaître, T. Ozawa, L. Le Gratiet, I. Sagnes, J. Bloch, and A. Amo, Lasing in topological edge states of a one-dimensional lattice, *Nature Photonics* **11**, 651–656 (2017).
- [15] R. Süssstrunk and S. D. Huber, Observation of phononic helical edge states in a mechanical topological insulator, *Science* **349**, 47–50 (2015).
- [16] M. Atala, M. Aidelsburger, J. T. Barreiro, D. Abanin, T. Kitagawa, E. Demler, and I. Bloch, Direct measurement of the zak phase in topological bloch bands, *Nature Physics* **9**, 795 (2013).
- [17] M. Atala, M. Aidelsburger, M. Lohse, J. T. Barreiro, B. Paredes, and I. Bloch, Observation of chiral currents with ultracold atoms in bosonic ladders, *Nature Physics* **10**, 588 (2014).
- [18] B. K. Stuhl, H.-I. Lu, L. M. Aycock, D. Genkina, and I. B. Spielman, Visualizing edge states with an atomic bose gas in the quantum hall regime, *Science* **349**, 1514 (2015).
- [19] M. Mancini, G. Pagano, G. Cappellini, L. Livi, M. Rider, J. Catani, C. Sias, P. Zoller, M. Inguscio, M. Dalmonte, and L. Fallani, Observation of chiral edge states with neutral fermions in synthetic hall ribbons, *Science* **349**, 1510 (2015).
- [20] G. Jotzu, M. Messer, R. Desbuquois, M. Lebrat, T. Uehlinger, D. Greif, and T. Esslinger, Experimental realization of the topological haldane model with ultracold fermions, *Nature* **515**, 237–240 (2014).
- [21] M. Aidelsburger, M. Lohse, C. Schweizer, M. Atala, J. T. Barreiro, S. Nascimbène, N. R. Cooper, I. Bloch, and N. Goldman, Measuring the chern number of hofstadter bands with ultracold bosonic atoms, *Nature Physics* **11**, 162–166 (2014).
- [22] M. Lohse, C. Schweizer, O. Zilberberg, M. Aidelsburger, and I. Bloch, A thouless quantum pump with ultracold bosonic atoms in an optical superlattice, *Nature Physics* **12**, 350–354 (2015).
- [23] S. Nakajima, T. Tomita, S. Taie, T. Ichinose, H. Ozawa, L. Wang, M. Troyer, and Y. Takahashi, Topological thouless pumping of ultracold fermions, *Nature Physics* **12**, 296–300 (2016).
- [24] M. Aidelsburger, S. Nascimbene, and N. Goldman, Artificial gauge fields in materials and engineered systems, *Comptes Rendus Physique* **19**, 394 (2018), quantum simulation / Simulation quantique.
- [25] N. R. Cooper, J. Dalibard, and I. B. Spielman, Topological bands for ultracold atoms, *Rev. Mod. Phys.* **91**, 015005 (2019).
- [26] A. W. W. Ludwig, Topological phases: classification of topological insulators and superconductors of non-interacting fermions, and beyond, *Physica Scripta* **T168**, 014001 (2015).
- [27] C.-K. Chiu, J. C. Y. Teo, A. P. Schnyder, and S. Ryu, Classification of topological quantum matter with symmetries, *Rev. Mod. Phys.* **88**, 035005 (2016).
- [28] I. Bloch, J. Dalibard, and W. Zwerger, Many-body physics with ultracold gases, *Rev. Mod. Phys.* **80**, 885 (2008).
- [29] I. Bloch, J. Dalibard, and S. Nascimbène, Quantum simulations with ultracold quantum gases, *Nature Physics* **8**, 267 (2012).

- [30] C. Gross and I. Bloch, Quantum simulations with ultracold atoms in optical lattices, *Science* **357**, 995–1001 (2017).
- [31] F. Schäfer, T. Fukuhara, S. Sugawa, Y. Takasu, and Y. Takahashi, Tools for quantum simulation with ultracold atoms in optical lattices, *Nature Reviews Physics* **2**, 411–425 (2020).
- [32] A. Browaeys and T. Lahaye, Many-body physics with individually controlled rydberg atoms, *Nature Physics* **16**, 132 (2020).
- [33] N. Goldman, J. C. Budich, and P. Zoller, Topological quantum matter with ultracold gases in optical lattices, *Nature Physics* **12**, 639 (2016).
- [34] D.-W. Zhang, Y.-Q. Zhu, Y. X. Zhao, H. Yan, and S.-L. Zhu, Topological quantum matter with cold atoms, *Advances in Physics* **67**, 253–402 (2018).
- [35] W. S. Bakr, J. I. Gillen, A. Peng, S. Fölling, and M. Greiner, A quantum gas microscope for detecting single atoms in a hubbard-regime optical lattice, *Nature* **462**, 74–77 (2009).
- [36] J. F. Sherson, C. Weitenberg, M. Endres, M. Cheneau, I. Bloch, and S. Kuhr, Single-atom-resolved fluorescence imaging of an atomic mott insulator, *Nature* **467**, 68–72 (2010).
- [37] L. W. Cheuk, M. A. Nichols, M. Okan, T. Gersdorf, V. V. Ramasesh, W. S. Bakr, T. Lompe, and M. W. Zwierlein, Quantum-gas microscope for fermionic atoms, *Phys. Rev. Lett.* **114**, 193001 (2015).
- [38] E. Haller, J. Hudson, A. Kelly, D. A. Cotta, B. Peaudecerf, G. D. Bruce, and S. Kuhr, Single-atom imaging of fermions in a quantum-gas microscope, *Nature Physics* **11**, 738 (2015).
- [39] M. F. Parsons, F. Huber, A. Mazurenko, C. S. Chiu, W. Setiawan, K. Wooley-Brown, S. Blatt, and M. Greiner, Site-resolved imaging of fermionic ${}^6\text{Li}$ in an optical lattice, *Phys. Rev. Lett.* **114**, 213002 (2015).
- [40] G. J. A. Edge, R. Anderson, D. Jervis, D. C. McKay, R. Day, S. Trotzky, and J. H. Thywissen, Imaging and addressing of individual fermionic atoms in an optical lattice, *Phys. Rev. A* **92**, 063406 (2015).
- [41] M. Boll, T. A. Hilker, G. Salomon, A. Omran, J. Nespolo, L. Pollet, I. Bloch, and C. Gross, Spin- and density-resolved microscopy of antiferromagnetic correlations in fermi-hubbard chains, *Science* **353**, 1257–1260 (2016).
- [42] C. Gross and W. S. Bakr, Quantum gas microscopy for single atom and spin detection, *Nature Physics* **17**, 1316 (2021).
- [43] C. Braun, R. Saint-Jalm, A. Hesse, J. Arceri, I. Bloch, and M. Aidelsburger, Real-space detection and manipulation of topological edge modes with ultracold atoms, *Nature Physics* [10.1038/s41567-024-02506-z](https://doi.org/10.1038/s41567-024-02506-z) (2024).
- [44] W. P. Su, J. R. Schrieffer, and A. J. Heeger, Solitons in polyacetylene, *Phys. Rev. Lett.* **42**, 1698 (1979).
- [45] S. de Léséleuc, V. Lienhard, P. Scholl, D. Barredo, S. Weber, N. Lang, H. P. Büchler, T. Lahaye, and A. Browaeys, Observation of a symmetry-protected topological phase of interacting bosons with rydberg atoms, *Science* **365**, 775 (2019).
- [46] J. Léonard, S. Kim, J. Kwan, P. Segura, F. Grusdt, C. Repellin, N. Goldman, and M. Greiner, Realization of a fractional quantum hall state with ultracold atoms, *Nature* **619**, 495 (2023).
- [47] P. Lunt, P. Hill, J. Reiter, P. M. Preiss, M. Gałka, and S. Jochim, Realization of a Laughlin state of two rapidly rotating fermions, arXiv [10.48550/arXiv.2402.14814](https://arxiv.org/abs/10.48550/arXiv.2402.14814) (2024), [2402.14814](https://arxiv.org/abs/2402.14814).
- [48] F. D. M. Haldane, Nonlinear field theory of large-spin heisenberg antiferromagnets: Semiclassically quantized solitons of the one-dimensional easy-axis néel state, *Phys. Rev. Lett.* **50**, 1153 (1983).
- [49] P. Sompet, S. Hirthe, D. Bourgund, T. Chalopin, J. Bibo, J. Koepsell, P. Bojović, R. Verresen, F. Pollmann, G. Salomon, C. Gross, T. A. Hilker, and I. Bloch, Realizing the symmetry-protected haldane phase in fermi-hubbard ladders, *Nature* **606**, 484 (2022).
- [50] T. Langen, R. Geiger, and J. Schmiedmayer, Ultracold atoms out of equilibrium, *Annual Review of Condensed Matter Physics* **6**, 201 (2015).
- [51] A. P. Luca D’Alessio, Yariv Kafri and M. Rigol, From quantum chaos and eigenstate thermalization to statistical mechanics and thermodynamics, *Advances in Physics* **65**, 239 (2016).
- [52] E. Dagotto and T. M. Rice, Surprises on the way from one- to two-dimensional quantum magnets: The ladder materials, *Science* **271**, 618 (1996).
- [53] E. Dagotto, Experiments on ladders reveal a complex interplay between a spin-gapped normal state and superconductivity, *Reports on Progress in Physics* **62**, 1525–1571 (1999).
- [54] R. Steinigeweg, F. Heidrich-Meisner, J. Gemmer, K. Michielsen, and H. De Raedt, Scaling of diffusion constants in the spin- $\frac{1}{2}$ xx ladder, *Phys. Rev. B* **90**, 094417 (2014).
- [55] D. Schubert, J. Richter, F. Jin, K. Michielsen, H. De Raedt, and R. Steinigeweg, Quantum versus classical dynamics in spin models: Chains, ladders, and square lattices, *Phys. Rev. B* **104**, 054415 (2021).
- [56] T. Rakovszky, C. W. von Keyserlingk, and F. Pollmann, Dissipation-assisted operator evolution method for capturing hydrodynamic transport, *Phys. Rev. B* **105**, 075131 (2022).
- [57] G. A. Domínguez-Castro, T. Bilitewski, D. Wellnitz, A. M. Rey, and L. Santos, Relaxation in dipolar spin ladders: From pair production to false-vacuum decay, *Phys. Rev. A* **110**, L021302 (2024).
- [58] S. Hirthe, T. Chalopin, D. Bourgund, P. Bojović, A. Bohrdt, E. Demler, F. Grusdt, I. Bloch, and T. A. Hilker, Magnetically mediated hole pairing in fermionic ladders of ultracold atoms, *Nature* **613**, 463–467 (2023).
- [59] J. F. Wienand, S. Karch, A. Impertro, C. Schweizer, E. McCulloch, R. Vasseur, S. Gopalakrishnan, M. Aidelsburger, and I. Bloch, Emergence of fluctuating hydrodynamics in chaotic quantum systems, *Nature Physics* , 1 (2024).
- [60] M. Leder, C. Grossert, L. Sitta, M. Genske, A. Rosch, and M. Weitz, Real-space imaging of a topologically protected edge state with ultracold atoms in an amplitude-chirped optical lattice, *Nature Communications* **7**, 13112 (2016).
- [61] C. Poli, M. Bellec, U. Kuhl, F. Mortessagne, and H. Schomerus, Selective enhancement of topologically induced interface states in a dielectric resonator chain, *Nature Communications* **6**, 6710 (2015).
- [62] E. J. Meier, F. A. An, and B. Gadway, Observation of the topological soliton state in the su–schrieffer–heeger model, *Nature Communications* **7**, 13986 (2016).
- [63] W. Cai, J. Han, F. Mei, Y. Xu, Y. Ma, X. Li, H. Wang, Y. P. Song, Z.-Y. Xue, Z.-q. Yin, S. Jia, and L. Sun,

- Observation of topological magnon insulator states in a superconducting circuit, *Phys. Rev. Lett.* **123**, 080501 (2019).
- [64] S. Lin, L. Zhang, T. Tian, C.-K. Duan, and J. Du, Dynamic observation of topological soliton states in a programmable nanomechanical lattice, *Nano Letters* **21**, 1025 (2021).
- [65] See the Supplemental Material (at the url provided by the publisher) for a detailed discussion on the stability analysis of the DW in the hard-core regime, the defect theory explaining the staggered RRD correlations for $\eta > 2$, the topological edge modes, the non-topologically localized states, the stability of the DW against swaps $20 \rightarrow 02$, extended numerical results for lower η values, details on the MPS calculations, and defect-defect interactions.
- [66] Note that $J_{\perp}/U = 1/2$ lies clearly beyond the validity regime of perturbation theory, explaining why the localization in Fig. 4 (a) does not have zero localization length, as may have been expected from Eq. (5). However, the qualitative features of topological and non-topological localization remain valid.
- [67] Similar to defect creation $|2, 0\rangle \leftrightarrow |\pm, \pm\rangle$ is non-resonant due to the rung energy, and $|2, 0\rangle \leftrightarrow |\pm, \mp\rangle$, which would be resonant, cannot be induced by leg hopping due to leg exchange symmetry.
- [68] A. Impertro, S. Karch, J. F. Wienand, S. Huh, C. Schweizer, I. Bloch, and M. Aidelsburger, Local read-out and control of current and kinetic energy operators in optical lattices, *Phys. Rev. Lett.* **133**, 063401 (2024).
- [69] A. Smith, J. Knolle, D. L. Kovrizhin, and R. Moessner, Disorder-free localization, *Phys. Rev. Lett.* **118**, 266601 (2017).
- [70] S. Kolkowitz, S. L. Bromley, T. Bothwell, M. L. Wall, G. E. Marti, A. P. Koller, X. Zhang, A. M. Rey, and J. Ye, Spin-orbit-coupled fermions in an optical lattice clock, *Nature* **542**, 66–70 (2016).
- [71] T. Bilitewski and A. M. Rey, Manipulating growth and propagation of correlations in dipolar multilayers: From pair production to bosonic kitaev models, *Phys. Rev. Lett.* **131**, 053001 (2023).
- [72] G. Vidal, Efficient Simulation of One-Dimensional Quantum Many-Body Systems, *Phys. Rev. Lett.* **93**, 040502 (2004).
- [73] A. T. Sornborger and E. D. Stewart, Higher-order methods for simulations on quantum computers, *Phys. Rev. A* **60**, 1956 (1999).
- [74] J. Bezanson, A. Edelman, S. Karpinski, and V. B. Shah, Julia: A fresh approach to numerical computing, *SIAM review* **59**, 65 (2017).
- [75] M. Fishman, S. R. White, and E. M. Stoudenmire, The ITensor Software Library for Tensor Network Calculations, *SciPost Phys. Codebases* , 4 (2022).

Supplementary Information

This supplementary information contains additional details on the stability analysis of the DW in the hard-core regime, the defect theory explaining the staggered RDD correlations for $\eta > 2$, the topological edge modes, the non-topologically localized states, the stability of the DW against swaps $20 \rightarrow 02$, extended numerical results for lower η values, details on the MPS simulations and convergence with time-step and bond-dimension, and defect-defect interactions.

Stability analysis of the DW in the hard-core regime

We briefly discuss the stability of the DW in the hard-core regime against the creation of singlon defects via Bogoliubov analysis valid at small excitation density (see also Refs. [57, 71] for similar analyses).

We introduce the hard-core bosonic operators $a_{i,\alpha}^\dagger = b_{i,\alpha}^\dagger$ ($b_{i,\alpha}^\dagger$) for even (odd) i . The initial density wave is then mapped to a vacuum state, and the operators $a_{i,\alpha}^\dagger$ create an excitation on top of the DW, i.e. a hole (particle) in even (odd) rungs. Note that this is also equivalent to a Holstein-Primakov transformation when mapping the hard-core Bose-Hubbard ladder as an XX spin ladder. Denoting $a_{i,\pm} = (a_{i,1}^\dagger \pm a_{i,2}^\dagger)/\sqrt{2}$, we re-write the Hamiltonian \hat{H}_0 in the form $\hat{H}_0 = \hat{H}_+ + \hat{H}_-$, where

$$\hat{H}_\sigma = -\sum_i \left[\frac{\sigma J_\perp}{2} \hat{a}_{i,\sigma}^\dagger \hat{a}_{i,\sigma} - \frac{J_\parallel}{2} (\hat{a}_{i,\sigma}^\dagger \hat{a}_{i+1,\sigma}^\dagger + \text{H.c.}) \right]. \quad (\text{S1})$$

For a small density of excitations, we may neglect the hard-core character, and move to momentum space:

$$\hat{H}_\sigma = -\sum_k \left[\frac{\sigma J_\perp}{2} \hat{a}_{k,\sigma}^\dagger \hat{a}_{k,\sigma} - J_\parallel \cos k (\hat{a}_{k,\sigma}^\dagger \hat{a}_{-k,\sigma}^\dagger + \text{H.c.}) \right], \quad (\text{S2})$$

which may be diagonalized by means of a Bogoliubov transformation, resulting in the dispersion law

$$\xi(k) = \sqrt{J_\perp^2/4 - J_\parallel^2 \cos^2 k}. \quad (\text{S3})$$

Dynamical Bogoliubov instability is hence expected only for $J_\perp/J_\parallel < 2$, as discussed in the main text.

Defect theory explaining the staggered RDD correlations

In this section we provide a non-interacting description of the dynamics in the two-defect sector on top of the initial DW pattern to explain the observed staggered RDD correlations. To do so we will first derive the dynamics of two non-interacting defects, and then in a second step

explain how their propagation affects the RDD correlations.

Let us consider a pair of singlon defects, either $|+, +\rangle$ or $|-, -\rangle$, created by quantum fluctuations at neighboring rungs j and $j+1$. Once created by quantum fluctuations, the defects may move along the ladder by swapping with $|2\rangle$ or $|0\rangle$, resulting (for $U \rightarrow \infty$) in an effective hopping rate J_\parallel . Let us denote $|\phi_j\rangle$ as the state with a defect at rung j . The initial state of the pair is hence $|\phi_j, \phi_{j+1}\rangle$. We start by re-expressing this state in momentum space as

$$|\phi_j, \phi_{j+1}\rangle = \frac{1}{L} \sum_{k,k'} e^{i(kj+k'(j+1))} |\tilde{\phi}_k, \tilde{\phi}_{k'}\rangle. \quad (\text{S4})$$

Since $|\tilde{\phi}_k\rangle$ is an eigenstate of the leg hopping with eigenenergy $-J_\parallel \cos k$, the time-evolved state acquires the form

$$\begin{aligned} & \frac{1}{L} \sum_{k,k'} e^{i(kj+k'(j+1))} e^{iJ_\parallel t(\cos k + \cos k')} |\tilde{\phi}_k, \tilde{\phi}_{k'}\rangle \\ &= \frac{1}{L^2} \sum_{k,k',l,l'} e^{i(kj+k'(j+1))} e^{iJ_\parallel t(\cos k + \cos k')} e^{-i(kl+k'l')} |\phi_l, \phi_{l'}\rangle \\ &= \sum_{l,l'} (-1)^j i^{1-l-l'} \mathcal{J}_{j-l}(J_\parallel t) \mathcal{J}_{j+1-l'}(J_\parallel t) |\phi_l, \phi_{l'}\rangle. \end{aligned} \quad (\text{S5})$$

We assume that the pair is initially created with equal probability at any position. Hence, initially, $|\psi(0)\rangle = \frac{1}{\sqrt{L}} \sum_j |\phi_j, \phi_{j+1}\rangle$. Then, using that

$$\begin{aligned} & \sum_{j,l,l'} (-1)^j i^{1-l-l'} \mathcal{J}_{j-l}(J_\parallel t) \mathcal{J}_{j+1-l'}(J_\parallel t) \\ &= \sum_{l,l'} i^{1+l-l'} \mathcal{J}_{l-l-1}(2J_\parallel t), \end{aligned} \quad (\text{S6})$$

we obtain the two-defect state at time t :

$$|\psi(t)\rangle = \frac{1}{\sqrt{L}} \sum_{l,l' \neq l} i^{1-(l'-l)} \mathcal{J}_{(l'-l)-1}(2J_\parallel t) |\phi_l, \phi_{l'}\rangle \quad (\text{S7})$$

The probability to find a defect at rung l and the other at rung l' is then

$$P(l, l') = \frac{1}{L} \sum_{l,l' \neq l} \mathcal{J}_{(l'-l)-1}^2(2J_\parallel t). \quad (\text{S8})$$

Since this was derived for a pair-defect density of $1/L$, for the pair density of the order of $(J_\parallel/J_\perp)^2$, we obtain

$$P(l, l') \simeq \left(\frac{J_\parallel}{J_\perp} \right)^2 \sum_{l,l' \neq l} \mathcal{J}_{(l'-l)-1}^2(2J_\parallel t). \quad (\text{S9})$$

Hence, the number of defects at a distance r is given by

$$P(r) = L \left(\frac{J_\parallel}{J_\perp} \right)^2 \mathcal{J}_{|r|-1}^2(2J_\parallel t) \quad (\text{S10})$$

We now turn to how these dynamics affect the background DW pattern and in turn the RDD correlations. Each time a defect moves it displaces a $|0\rangle$ or a $|2\rangle$. As a result, the region between the two defects consists of a string of sites with the DW pattern inverted compared to the initial state, i.e. a $|0\rangle$ becomes a $|2\rangle$, and vice versa (see Fig. 2(c) of the main text).

In order to understand why this results in staggered RDD correlations, let us consider two rungs, for example $i = 0$ (an even rung), and $j = r$, which may be even or odd. Although cumbersome, one can easily identify which changes occur in the occupations of those rungs, and with which probability they happen, when the pair of defects moves across those rungs. We employ in the following the notation (Change(i), Change(j)), where Change may be either "=" (i.e. no change), 1 (one particle in the rung), or Flip (i.e. $|0\rangle \leftrightarrow |2\rangle$). These are the possible changes, and their probabilities:

- (1, =) or (=, 1); $\sum_{l>0} P(l) + \sum_{0<l<r} P(l)$
- (Flip, =) or (=, Flip); $\sum_{l>0} \sum_{0<l'<r} P(l+l')$
- (Flip, 1) or (1, Flip); $\sum_{l>0} P(l+r)$
- (Flip, Flip); $\sum_{l>0} \sum_{l'>0} P(l+l'+r)$
- (1, 1); $P(r)$

Each change affects the RDD correlations. After some tedious calculation one obtains:

$$\begin{aligned}
 C_{0,r}(t) &= (-1)^r \left[4 \sum_{j>0} j P(j+r, t) + P(r, t) \right] \\
 &= 2(-1)^r \left(\frac{J_{\parallel}}{J_{\perp}} \right)^2 \left[4 \sum_{j>0} j \mathcal{J}_{j+r-1} (2J_{\parallel}t)^2 + \mathcal{J}_{r-1} (2J_{\parallel}t)^2 \right] \quad (\text{S11})
 \end{aligned}$$

This expression corresponds to a ballistically-expanding cone of staggered correlations, which matches well with the numerical results of Fig. 2(d).

Topological edge modes and localisation

In this section we provide the derivation for the topological edge modes appearing in the effective SSH model for single defect dynamics.

Let us consider the effective SSH model of Eq. (4) of the main text. We can divide the lattice into A and B sublattice, such that $|m, A\rangle$ ($|m, B\rangle$) is the A (B) rung in the m -th elementary cell. The defect is initially in $|0, A\rangle$.

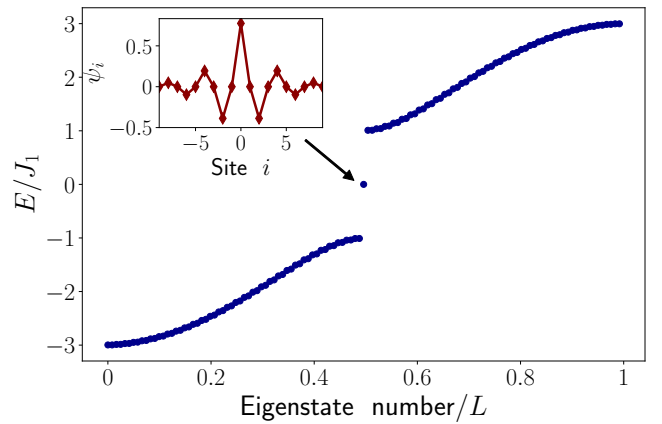


FIG. S1. Eigenspectrum of the SSH model of Eq. (4) of the main text, when $J_2 = 2J_1$. The inset shows the wavefunction ψ_i at site i (with $i = 0$ the initial defect position) of the topological zero-energy edge mode. Note that the mode occupies only sublattice A (even sites).

We can then rewrite the Hamiltonian in the form:

$$\begin{aligned}
 \hat{H} &= -\frac{J_1}{2} \sum_{m \geq 0} [|m, A\rangle \langle m, B| + |m, B\rangle \langle m, A|] \\
 &\quad -\frac{J_2}{2} \sum_{m < 0} [|m, A\rangle \langle m, B| + |m, B\rangle \langle m, A|] \\
 &\quad -\frac{J_2}{2} \sum_{m \geq 0} [|m+1, A\rangle \langle m, B| + |m, B\rangle \langle m+1, A|] \\
 &\quad -\frac{J_1}{2} \sum_{m < 0} [|m+1, A\rangle \langle m, B| + |m, B\rangle \langle m+1, A|] \quad (\text{S12})
 \end{aligned}$$

We consider first the case $J_1 < J_2$. As shown in Fig. S1 the eigenspectrum of this model presents a topological zero-energy mode at the interface between the two SSH chains. In order to understand the properties of this edge mode, let us consider a state $|\psi\rangle = \sum_m [a_m |m, A\rangle + b_m |m, B\rangle]$. If this state is the topological edge state with eigenstate $E = 0$, then $\hat{H}|\psi\rangle = 0$, which leads to the recursions:

- For $m \geq 0$, $a_{m+1} = -\frac{J_1}{J_2} a_m$
- For $m < 0$, $a_{m-1} = -\frac{J_1}{J_2} a_m$
- $b_0 + b_{-1} = 0$
- For $m \geq 0$: $b_{m+1} = -\frac{J_2}{J_1} b_m$
- For $m < 0$: $b_{m-1} = -\frac{J_2}{J_1} b_m$

Then: $a_m = \left(-\frac{J_1}{J_2}\right)^{|m|} a_0$, and $b_{m \geq 0} = \left(-\frac{J_2}{J_1}\right)^m b_0 = -b_{-(m+1)}$. If $J_1/J_2 < 1$, we can define $J_1/J_2 \equiv e^{-1/2\xi}$, such that $|a_m|^2 = e^{-|m|/\xi} |a_0|^2$ and $|b_{m \geq 0}|^2 = e^{m/\xi} |b_0|^2 = |b_{-(m+1)}|^2$. Since the solution must be normalized, this

means that the physical solution must have $b_0 = 0$, and hence the localized edge mode lives only in the A sublattice: $|\psi\rangle = a_0 \sum_m e^{-|m|/2\xi} |m, A\rangle$. We illustrate this localised state in the inset of Fig. S1.

To connect with the expansion dynamics of an initially localised defect, starting with $|0, A\rangle$ we expect that a probability given by $P_0 = |a_0|^2$ remains localized in the edge state, which lives only in the A sublattice. The value of the localized fraction P_0 is easily found by normalization:

$$P_0 = \frac{J_2^2 - J_1^2}{J_2^2 + J_1^2}. \quad (\text{S13})$$

Non topological localized states

Next we consider $J_1 > J_2$, in which a defect on the A sublattice turns out to be non-topologically localised.

The corresponding eigenspectrum is depicted in Fig. S2 (d). The same analysis as in the previous section shows that for $J_1 > J_2$ the zero-energy topological edge mode only occupies sublattice B, see Fig. S2 (b), and, thus, is not relevant to the dynamics of a defect initially on the A sublattice. However two other localized modes, which have overlap with the central site, appear at both ends of the eigenspectrum, see Fig. S2 (a) and (c).

In order to understand the properties of those localized states, we define $|\alpha_0\rangle \equiv |0, A\rangle$, $|\alpha_{m>0}\rangle \equiv \frac{|m, A\rangle + | -m, A\rangle}{\sqrt{2}}$, and $|\beta_{m\geq 0}\rangle \equiv \frac{|m, B\rangle + | -(m+1), B\rangle}{\sqrt{2}}$. Let us consider states $|\psi\rangle = \sum_{m\geq 0} (\alpha_m |\alpha_m\rangle + \beta_m |\beta_m\rangle)$. For the states of interest, i.e. the manifold of states that may be reached from $|0, A\rangle$, we can define the Hamiltonian:

$$\begin{aligned} \hat{H} &= -\sqrt{2} \frac{J_1}{2} (|\alpha_0\rangle\langle\beta_0| + \text{H.c.}) \\ &- \frac{J_2}{2} \sum_{m\geq 0} (|\beta_m\rangle\langle\alpha_{m+1}| + \text{H.c.}) \\ &- \frac{J_1}{2} \sum_{m>0} (|\alpha_m\rangle\langle\beta_m| + \text{H.c.}). \end{aligned} \quad (\text{S14})$$

Let $|S_m\rangle \equiv \frac{|\alpha_m\rangle + |\beta_m\rangle}{\sqrt{2}}$, and $|A_m\rangle \equiv \frac{|\alpha_m\rangle - |\beta_m\rangle}{\sqrt{2}}$, then:

$$\begin{aligned} \hat{H} &= -\sqrt{2} \frac{J_1}{2} (|S_0\rangle\langle S_0| - |A_0\rangle\langle A_0|) \\ &- \frac{J_1}{2} \sum_{m>0} (|S_m\rangle\langle S_m| - |A_m\rangle\langle A_m|) \\ &- \frac{J_2}{4} \sum_{m\geq 0} (|S_m\rangle\langle S_{m+1}| - |A_m\rangle\langle A_{m+1}| \\ &+ |S_m\rangle\langle A_{m+1}| - |A_m\rangle\langle S_{m+1}| + \text{H.c.}). \end{aligned} \quad (\text{S15})$$

Assuming $J_2/J_1 \ll 2(\sqrt{2} - 1)$, we can neglect the coupling between A and S states, and hence obtain

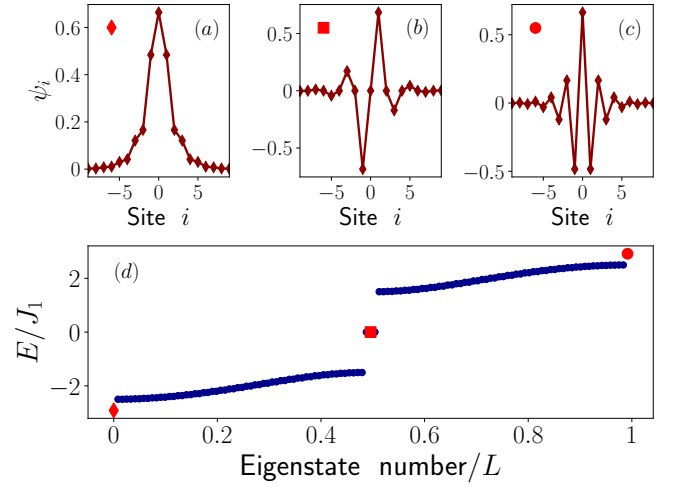


FIG. S2. (a-c) Wavefunction ψ_i at site i (with $i = 0$ the initial defect position) of the localized eigenstates of model (4) of the main text, when $J_1 = 2J_2$. (d) Eigenspectrum of the model, where we have indicated with different symbols the energies of the localized states depicted in panels (a-c). The zero-energy mode only exists in sublattice B (odd rungs). The other localized solutions correspond to eigenstates at both ends of the spectrum. Note that ψ_i in panel (a) corresponds to $(-1)^i \psi_i$ in panel (c).

$\hat{H} \simeq \hat{H}_S + \hat{H}_A$, with

$$\begin{aligned} \hat{H}_S &= -\sqrt{2} \frac{J_1}{2} |S_0\rangle\langle S_0| - \frac{J_1}{2} \sum_{m>0} |S_m\rangle\langle S_m| \\ &- \frac{J_2}{4} \sum_{m\geq 0} |S_m\rangle\langle S_{m+1}| + \text{H.c.} \end{aligned} \quad (\text{S16})$$

and \hat{H}_A is the same with an overall minus. We can remove the identity $-J_1 \mathbf{1}$, obtaining the final expression

$$\begin{aligned} \hat{H}_S &= -(\sqrt{2} - 1) \frac{J_1}{2} |S_0\rangle\langle S_0| \\ &- \frac{J_2}{4} \sum_{m\geq 0} (|S_m\rangle\langle S_{m+1}| + \text{H.c.}), \end{aligned} \quad (\text{S17})$$

which describes a semi-infinite lattice with a defect in the first site.

Let us assume an exponentially localized solution $|\psi_S\rangle = \mathcal{N} \sum_{m\geq 0} e^{-m/2\xi} |S_m\rangle$, where the normalization \mathcal{N}^2 is the probability to be in $|S_0\rangle$. This solution has an energy $E = -\sqrt{2} \frac{J_1}{2} - \frac{J_2}{4} e^{-1/2\xi}$, where we restored the $-J_1$ we had dropped. On the other hand, second-order perturbation on top of the solution $|S_0\rangle$, gives the energy

$$E \simeq -\sqrt{2} \frac{J_1}{2} - \frac{J_2^2/2}{(\sqrt{2} - 1)J_1}. \quad (\text{S18})$$

We can hence approximate $e^{-1/2\xi} \simeq \frac{J_2/J_1}{2(\sqrt{2}-1)}$. Since

$\mathcal{N}^2 = 1 - e^{-1/\xi}$, we obtain

$$\mathcal{N}^2 = 1 - \left(\frac{J_2/J_1}{2(\sqrt{2}-1)} \right)^2. \quad (\text{S19})$$

This then fully determines the localized states discussed in the main text.

Note that the localized states at both ends are such that the state $\psi_i^{(E<0)}$ with energy $E < 0$ and the states $\psi_i(E > 0)$ with energy $E > 0$ fulfill $\psi_i^{(E<0)} = (-1)^i \psi_i^{(E>0)}$. As a result a linear combination $\psi_i^{(E<0)} + \psi_i^{(E>0)}$ oscillates with frequency $\Omega = E/\hbar$ between the A and the B sublattice, as described in the main text.

Stability of the DW against $20 \rightarrow 02$ swaps

We project the second-order Hamiltonian \hat{H}_{eff} , see Eq. (1) and Eq. (3), into the manifold without singlon defects (doublon-holon manifold).

The case of neighboring doubly-occupied rungs (doublons) is simple since \hat{H}_{eff} does act diagonally on that state

$$\hat{H}_{\text{eff}}|2, 2\rangle = -\frac{2J_{\parallel}^2}{U}|2, 2\rangle, \quad (\text{S20})$$

where we disregard the rung energy because it will be a constant in the doublon-holon manifold.

Let us consider now a neighboring doublon-holon pair, i.e. $|2, 0\rangle$. Let us split the $\hat{H}_{\text{eff}} = \hat{H}_{\text{eff},0} + \hat{H}_{\text{eff},1}$, where

$$\hat{H}_{\text{eff},0} = -\frac{J_{\perp}}{2} \sum_j \left(\hat{b}_{j,1}^{\dagger} \hat{b}_{j,2} + \text{H.c.} \right) - \frac{J_{\perp}^2}{U} \sum_j \hat{n}_{j,1} \hat{n}_{j,2}, \quad (\text{S21})$$

is the rung energy. Note that $\hat{H}_{\text{eff},0}|2\rangle = -\frac{J_{\perp}^2}{U}|2\rangle$, $\hat{H}_{\text{eff},0}|\pm\rangle = \mp \frac{J_{\perp}}{2}|\pm\rangle$, and $\hat{H}_{\text{eff},0}|0\rangle = 0$. We consider $\hat{H}_{\text{eff},1}$ as a perturbation to $\hat{H}_{\text{eff},0}$. Then:

$$\begin{aligned} \hat{H}_{\text{eff},1}|\pm, \pm\rangle &= -\frac{J_{\parallel}^2}{2U} (|+, +\rangle + |-, -\rangle) \\ &\mp \frac{J_{\parallel}}{2} \left(1 \pm \frac{J_{\perp}}{U} \right) (|2, 0\rangle + |0, 2\rangle) \end{aligned} \quad (\text{S22})$$

$$\begin{aligned} \hat{H}_{\text{eff},1}|2, 0\rangle &= -\frac{J_{\parallel}}{2} \left(1 + \frac{J_{\perp}}{U} \right) |+, +\rangle \\ &+ \frac{J_{\parallel}}{2} \left(1 - \frac{J_{\perp}}{U} \right) |-, -\rangle. \end{aligned} \quad (\text{S23})$$

We can then easily evaluate the second-order processes:

$$\begin{aligned} &\hat{H}^{(2)}|2, 0\rangle \\ &= \left[\frac{J_{\parallel}^2(1+J_{\perp}/U)^2}{4(J_{\perp}-J_{\perp}^2/U)} - \frac{J_{\parallel}^2(1-J_{\perp}/U)^2}{4(J_{\perp}+J_{\perp}^2/U)} \right] (|2, 0\rangle + |0, 2\rangle) \\ &\simeq \frac{3J_{\parallel}^2}{2U} (|2, 0\rangle + |0, 2\rangle), \end{aligned} \quad (\text{S24})$$

where we assume $J_{\perp}/U \ll 1$. Note that although the result for $\hat{H}^{(2)}|2, 0\rangle$ only depends on J_{\parallel}^2/U , it stems from assuming that J_{\perp} is much larger than any energy that can take out from the doublon-holon manifold.

We can then write the Hamiltonian for the manifold with only doublons and holons in the following way:

$$\begin{aligned} \hat{H}_D &= \frac{3J_{\parallel}^2}{2U} \sum_j \left[(\hat{d}_j^{\dagger} \hat{h}_j)(\hat{h}_{j+1}^{\dagger} \hat{d}_{j+1}) + (\hat{h}_j^{\dagger} \hat{d}_j)(\hat{d}_{j+1}^{\dagger} \hat{h}_{j+1}) \right] \\ &- \frac{2J_{\parallel}^2}{U} \sum_j \hat{n}_{d,j} \hat{n}_{d,j+1} \\ &+ \frac{3J_{\parallel}^2}{2U} \sum_j (\hat{n}_{d,j} \hat{n}_{h,j+1} + \hat{n}_{h,j} \hat{n}_{d,j+1}), \end{aligned} \quad (\text{S25})$$

where \hat{d}_j (\hat{h}_j) destroys a doublon (holon) at rung j , $\hat{n}_{d,j} = \hat{d}_j^{\dagger} \hat{d}_j$, $\hat{n}_{h,j} = \hat{h}_j^{\dagger} \hat{h}_j$, and $\hat{n}_{d,j} + \hat{n}_{h,j} = 1$. Note that there is no term arising from the collisionally-assisted next-to-NN hops, since that term would lead to the destruction of doublons and holons, which would take the system out the doublon-holon manifold. Since, destroying (creating) a doublon implies creating (destroying) a holon, since $\hat{n}_{h,j} = 1 - \hat{n}_{d,j}$, and since the number of holons and doublons is conserved, we may rewrite:

$$\hat{H}_D = \frac{3J_{\parallel}^2}{2U} \sum_j \left(\hat{d}_j^{\dagger} \hat{d}_{j+1} + \hat{d}_{j+1}^{\dagger} \hat{d}_j - \frac{10}{3} \hat{n}_{d,j} \hat{n}_{d,j+1} \right), \quad (\text{S26})$$

which is the expression written in the main text.

The relatively strong NN interaction between doubly-occupied sites is crucial for the DW stability. Considering an initial perfect DW with doubly-occupied even rungs, we introduce the operators that characterize alterations (DW-defects) of the initial DW order (i.e. a $|2\rangle$ ($|0\rangle$) where there should be a $|0\rangle$ ($|2\rangle$): $\hat{c}_j = \hat{d}_j^{\dagger}$ (\hat{d}_j) and $\hat{n}_{c,j} = 1 - \hat{n}_{d,j}$ ($\hat{n}_{d,j}$) for even (odd) j . This transforms the Hamiltonian into:

$$\begin{aligned} \hat{H}_{DH} &= \frac{3J_{\parallel}^2}{2U} \sum_j \left(\hat{c}_j^{\dagger} \hat{c}_{j+1}^{\dagger} + \hat{c}_j \hat{c}_{j+1} \right. \\ &\left. + \frac{10}{3} (1/2 - \hat{n}_{c,j})(1/2 - \hat{n}_{c,j+1}) \right). \end{aligned} \quad (\text{S27})$$

Assuming a dilute gas of DW-defects, we may neglect the defect-defect interaction, and removing constants we get:

$$\hat{H}_{DH} = \frac{3J_{\parallel}^2}{2U} \sum_j \left(\hat{c}_j^{\dagger} \hat{c}_{j+1}^{\dagger} + \hat{c}_j \hat{c}_{j+1} + \frac{10}{3} \hat{c}_j^{\dagger} \hat{c}_j \right) \quad (\text{S28})$$

Moving to momentum representation:

$$\begin{aligned} \hat{H} &= \frac{3J_{\parallel}^2}{2U} \sum_{k>0} \left[2 \cos(k) \left(\hat{c}_k^{\dagger} \hat{c}_{-k}^{\dagger} + \hat{c}_k \hat{c}_{-k} \right) \right. \\ &\left. + \frac{10}{3} \left(\hat{c}_k^{\dagger} \hat{c}_k + \hat{c}_{-k}^{\dagger} \hat{c}_{-k} \right) \right]. \end{aligned} \quad (\text{S29})$$

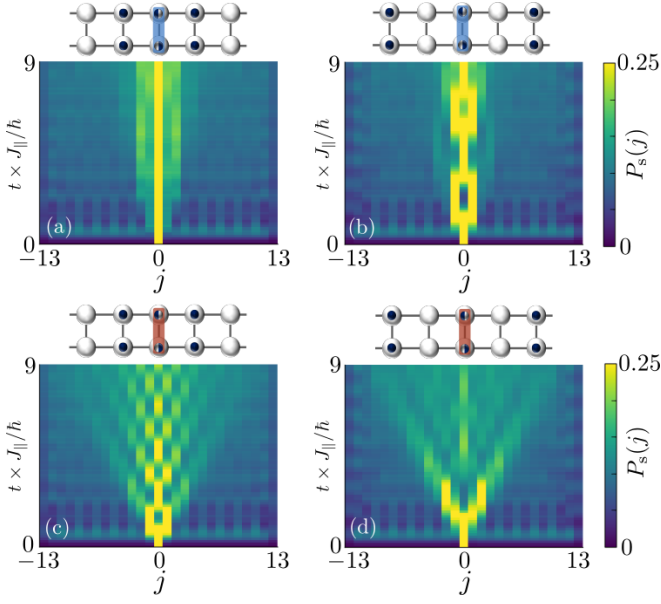


FIG. S3. Defect motion for $\eta = 8$, $U/J_{\parallel} = 16$, otherwise same as Fig. 4 of the main text. When reducing η , perturbative creation of defects is less suppressed. As a consequence, a background of singlon defects forms, but despite this background localization remains clearly visible.

Let $\hat{\beta}_k = u_k \hat{c}_k - v_k \hat{c}_{-k}^{\dagger}$, we impose $\xi \hat{\beta}_k = [\hat{H}_{DH}, \hat{\beta}_k]$, which leads to the Bogoliubov-de Gennes equations:

$$\begin{aligned} \xi(k)u_k &= \frac{3J_{\parallel}^2}{2U} \left[\frac{10}{3}u_k - 2\cos(k)v_k \right], \\ \xi(k)v_k &= \frac{3J_{\parallel}^2}{2U} \left[2\cos(k)u_k - \frac{10}{3}v_k \right], \end{aligned}$$

Diagonalizing the Bogoliubov-de Gennes matrix, we obtain the dispersion:

$$\xi(k) = \frac{3J_{\parallel}^2}{U} \sqrt{\left(\frac{5}{3}\right)^2 - \cos^2 k}. \quad (\text{S30})$$

Therefore, irrespective of k , the dispersion remains real,

$$(1)^T(1)(1)^T(-2)(1)^T(1)^T(1)^T(1)^T(1)(1)^T(1)(1)(1)(-2)^T(1)(1)^T(1). \quad (\text{S31})$$

Here, $(1)^T$ signifies applying the gates from the leftmost site of the MPS to the rightmost site, (1) signifies the reverse order, and $(-2)/(-2)^T$ are Trotter steps with a time step $-2dt$. Our simulation enforces the conservation of the number of particles. It is written in the julia programming language [74] and builds on the ITensor

and hence the DW is Bogoliubov stable against the formation of DW-defects.

Singlon-defect localization despite fluctuations of the DW pattern

In this section we address the robustness of the described phenomenology of topological and non-topological localisation obtained within the single defect effective SSH model to relevant fluctuations of the background pattern.

As mentioned in the main text, although the DW is stable against the creation of singlon defects, a small density of defects of the order of $1/\eta^2$ is created by quantum fluctuations, which creates pairs $|+, +\rangle$ and $|-, -\rangle$. As the ratio η decreases, a growing background of quantum defects develops. Fig. S3 shows that even in the presence of a small fraction of quantum singlon-defect pairs, localization remains stable at experimentally relevant times for $\eta = 8$ and $U/J_{\parallel} = 16$.

MPS simulations

We now describe the matrix product state simulation of the full Bose-Hubbard model. We represent the ladder as a one-dimensional matrix product state (MPS) by snaking through the ladder as $(i, \alpha) \rightarrow s = 2i + \alpha$. Since the bosons are strongly interacting, we truncate the bosonic Hilbert space to at most two bosons per lattice site. We use the time-evolving block decimation (TEBD) to compute time evolution of the state [72]. This approach is based on decomposing the Hamiltonian into two-site gates acting on nearest neighbors. To include tunneling along the ladder legs, we include swap gates along the rungs. We further include on-site interactions and rung tunneling in the same two-site Hamiltonian to reduce Trotter errors. We use a 4th order Trotter decomposition [73], allowing reasonably-sized time steps even in the presence of fast on-site interactions. In particular, we use the decomposition

package [75].

To test convergence with both time step and bond dimension, we repeat the simulations with a smaller bond dimension and larger time step and confirm that all plots remain virtually indistinguishable. In particular, we change the time step between $J_{\parallel}dt/\hbar = 2\pi \times 0.02/12$ and $J_{\parallel}dt/\hbar = 2\pi \times 0.04/12$, and iteratively change the bond

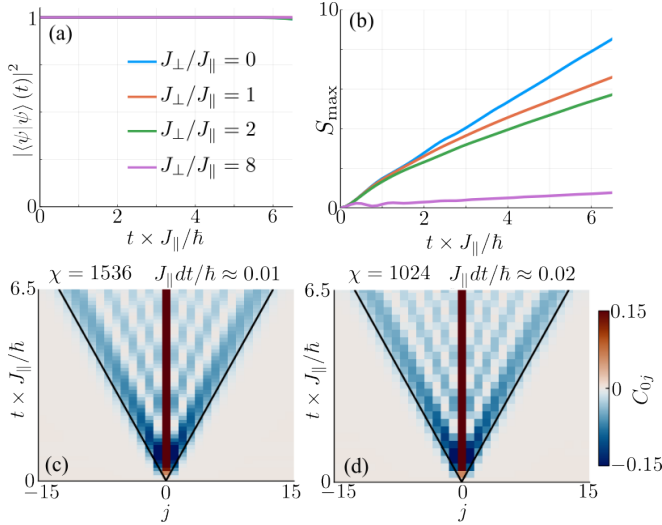


FIG. S4. Convergence of MPS data corresponding to Fig. 2. (a) Square of the state norm for the different ratios of J_{\perp}/J_{\parallel} . The curves overlap almost perfectly. (b) Maximal bipartite entanglement entropy for any MPS bipartition for different ratios of J_{\perp}/J_{\parallel} . (c/d) Demonstration of convergence by plotting rung-rung correlations for two different bond dimensions in the worst-case scenario (largest entropy).

dimension as $\chi = 128, 256, 512, 768, 1024, 1536$. The results of this procedure are shown in Fig. S4(c/d) for the data corresponding to Fig. 2 of the main text, and in Fig. S5(c/d) for the data corresponding to Fig. 4. Other than blurring out due to worse time resolution, there is no visible change between the plots.

We further test convergence with the bond dimension χ via the state norm and the entropy. For each applied gate, TEBD performs a singular value decomposition and truncates the smallest singular values after a given bond dimension. This procedure reduces the state norm by the square of the truncated singular values. Therefore, as long as the norm remains close to one, the state is barely truncated, and the MPS is likely a faithful representation of the true state. The state norm as a function of time is shown in Fig. S4(a) and Fig. S5(a) and remains well above 0.9 in all cases, indicating that the results are indeed converged. As a leading order corrections, whenever we compute observables, we divide the result by the state norm. In addition, we keep track of the maximal entanglement entropy for each bipartition of the chain throughout the evolution. The entropy is upper-bounded by the bond dimension χ as $S_{\max} \leq \log_2(\chi)$, and for convergence one typically wants $\chi \gg 2^{S_{\max}}$. This is the case for all parameters analyzed. Finally, we also confirmed the convergence of the entanglement entropy with bond dimension and found that it changes by at most 0.1 for all cases when decreasing the bond dimension in the above-mentioned steps (not shown). This indicates that all results are fully converged.

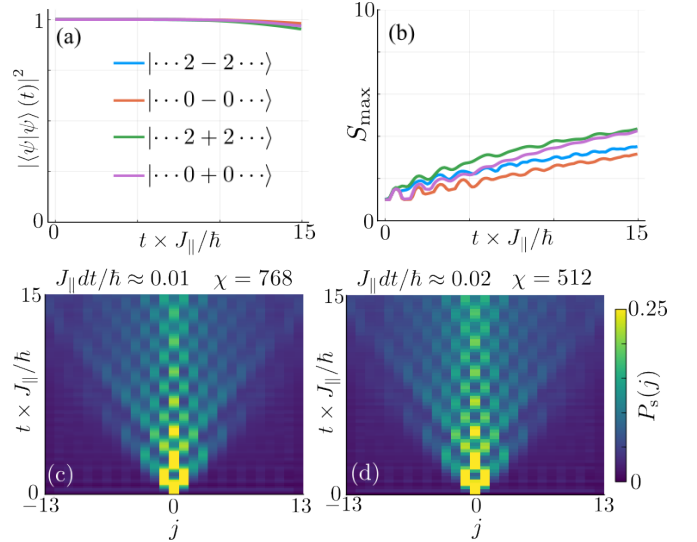


FIG. S5. Convergence of MPS data corresponding to Fig. 4. (a) Square of the state norm for the different initial defects. (b) Half-chain entanglement entropy for the different initial defects. The cut along which the entanglement entropy is considered is shown as a dotted line in the inset. (c/d) Demonstration of convergence by plotting rung-rung correlations for two different time steps in the worst-case scenario (largest entropy).

Defect-defect interactions

In the effective model, all singlon defect collisions are elastic and thus leave the physics discussed in the paper largely unperturbed. While inelastic $|+, +\rangle$ and $|-, -\rangle$ collisions are energetically suppressed, inelastic $|-, +\rangle$ transitions are forbidden by leg exchange symmetry. The only inelastic process is the perturbatively slow swap $|-, +\rangle \leftrightarrow |+, -\rangle$ at rate $J_{\parallel}^2/2U$.

In Fig. S6, we numerically verify that indeed $|-, +\rangle$ collisions do not significantly alter the conclusions drawn in the paper, such that they will be observable even in the presence of background defects. We initialize a $|-\rangle$ and a $|+\rangle$ defect separated by one site as shown in the top row. We then consider the time evolution of the probability to find a $|-\rangle$ or $|+\rangle$ defect independently in (a,b) and (c,d) for each initial configuration. In both cases, the $|-\rangle$ defect remains in the left half of the system, while the $|+\rangle$ defect remains in the right half, indicating that indeed swapping of the two defects is slow compared to the time scales of interest. Furthermore, the $|-\rangle$ state remains strongly localized in both cases despite the presence of a second defect.

Panels (e) and (f) show the total number of $|-\rangle$ and $|+\rangle$ defects in the chain. As predicted by the perturbative calculation, pair-annihilation of $|-\rangle$ and $|+\rangle$ defects is very inefficient since both \mathcal{N}_+ and \mathcal{N}_- drop barely below one. These results also show a stark difference in the number of $|+\rangle$ and $|-\rangle$ defects which are dynamically

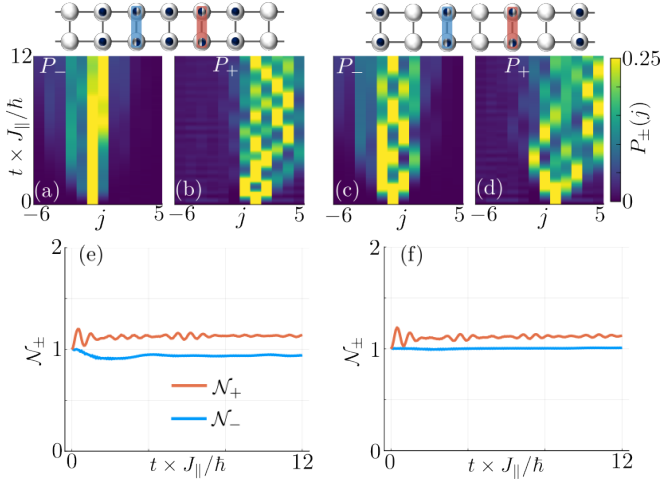


FIG. S6. Collision of two defects. (a)-(d) Probabilities to find each singlon defect in the different rungs for an initial singlon defect arrangement shown in the top row (identical for (a) and (b), and (c) and (d), respectively). (e) Cumulative number of singlon defects in the entire chain for the arrangement in (a/b). (f) Cumulative number of singlon defects in the entire chain for the arrangement in (c/d). Parameters: $\eta = 16$, $U/J_{\parallel} = 32$, bond dimension $\chi = 512$, chain length $L = 12$.

created from the background. This is explained by a difference in the effective creation rates Eq. (S23), and the smaller energetic cost for creating $|+\rangle$ defects due to the superexchange energy of the initial state $|2, 0\rangle$.